LANGMUIR Article
Cite This: Langmuir 2019, 35, 8716–8725
pubs.acs.org/Langmuir

Effects of Moisture Contents on Shale Gas Recovery and CO_2 Sequestration

Juan Zhou,[†,‡] Zhehui Jin,[*,‡] and Kai H. Luo[*,§]

[†]Center for Combustion Energy, Key Laboratory for Thermal Science and Power Engineering of Ministry of Education, Department of Energy and Power Engineering, Tsinghua University, Beijing 100084, China

[‡]School of Mining and Petroleum Engineering, Department of Civil and Environmental Engineering, University of Alberta, Edmonton, Alberta T6G 1H9, Canada

[§]Department of Mechanical Engineering, University College London, Torrington Place, London WC1E 7JE, U.K.

Supporting Information

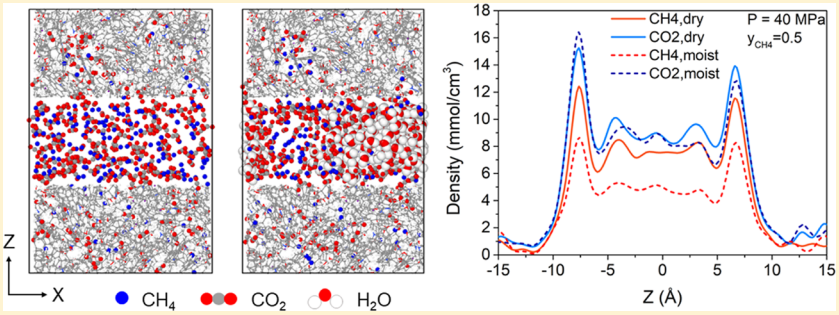

ABSTRACT: Enhanced recovery of shale gas with CO_2 injection has attracted extensive attention as it combines the advantages of improved efficiency of shale gas recovery and reduced greenhouse gas emissions via CO_2 geological sequestration. On the other hand, the microscopic mechanism of enhanced shale gas recovery with CO_2 injection and the influence of the subsurface water confined in the shale nanopores remain ambiguous. Here, we use grand canonical Monte Carlo (GCMC) simulations to investigate the effect of moisture on the shale gas recovery and CO_2 sequestration by calculating the adsorption of CH_4 and CO_2 in dry and moist kerogen slit pores. Simulation results indicate that water accumulates in the form of clusters in the middle of the kerogen slit pore. Formation of water clusters in kerogen slit pores reduces pore filling by methane molecules, resulting in a decrease in the methane sorption capacity. For the sorption of CH_4/CO_2 binary mixtures in kerogen slit pores, the CH_4 sorption capacity decreases as the moisture content increases, whereas the effect of moisture on CO_2 sorption capacity is related to its mole fraction in the CH_4/CO_2 binary mixture. Furthermore, we propose a reference route for shale gas recovery and find that the pressure drawdown and CO_2 injection exhibit different mechanisms for gas recovery. Pressure drawdown mainly extracts the CH_4 molecules distributed in the middle of kerogen slit pores, while CO_2 injection recovers CH_4 molecules from the adsorption layer. When the water content increases, the recovery ratio of the pressure drawdown declines, while that of CO_2 injection increases, especially in the first stage of CO_2 injection. The CO_2 sequestration efficiency is higher under higher water content. These findings provide the theoretical foundation for optimization of the shale gas recovery process, as well as effective CO_2 sequestration in depleted gas reservoirs.

1. INTRODUCTION

Shale gas, which predominantly consists of methane, has become an increasingly important energy source owing to its low emissions, high energy efficiency, and abundant reserves in the world.[1,2] In contrast to the conventional reservoirs, shale rocks have the characteristics of extremely low permeability in the nanodarcy range and low porosity.[3] The development of horizontal and hydraulic fracturing methods has greatly advanced shale gas exploitation in the United States.[4,5] Unfortunately, the widely used depressurization method becomes inefficient and significant amounts remain unrecoverable.[6] Recently, enhanced gas recovery (EGR) with CO_2 injection is considered to be a promising alternative that can not only enhance shale gas productivity but also mitigate the climate change via geological CO_2 sequestration,[7] in which CO_2 captured from power plants is injected into the shale gas reservoirs and sequestrated in a safe and permanent manner. The idea of swapping CO_2 for CH_4 can also be applied to other replacement reactions, such as the recovery of CH_4 from hydrate reservoirs.[8]

Kerogen makes up the major organic part of the shale rocks[9] and pores, mainly at the nanoscale, where a large amount of shale gas can be stored.[10] Therefore, it is crucial to understand the adsorption properties of CH_4 and CO_2 in kerogen in an

Received: March 23, 2019
Revised: June 4, 2019
Published: June 5, 2019

attempt to enhance the efficiency of shale gas recovery and CO_2 sequestration. It is also well known that shale is under moist conditions.[11−14] For example, kerogen from the Kuonamka Formation was reported to have moisture contents ranging from 0.6 to 5%.[11] Plenty of experimental work studied the effects of moisture on pure methane adsorption and suggested that the presence of water occupies the pore volume and thus leads to a sharp decrease in the methane adsorption capacity in shale.[14−17] On the other hand, relatively few experiments focused on the influence of moisture on the competitive adsorption of CH_4 and CO_2. Gensterblum et al.[18] investigated the effect of preadsorbed water on the CH_4 and CO_2 adsorption in coals and observed that the CO_2/CH_4 adsorption ratios at low surface coverage are generally higher in moist coals than in dry conditions, and with the presence of water, the mobility of CO_2 and CH_4 is reduced. Few laboratory studies have been reported on the competitive adsorption of CO_2 and CH_4 in the moist kerogen. Isolation of the kerogen from shale samples with the morphology of the kerogen intact remains challenging for experiments.[9] Moreover, shale rocks contain a large amount of nanoscaled pores, further increasing the difficulties of experimental approaches in probing the adsorption behaviors in shales.

Molecular simulations have been successfully applied to interfacial and colloid science,[19] including adsorption,[20−22] wetting,[23,24] and surfactants.[25] Much research in recent years has made significant progress in understanding the competitive adsorption of CH_4 and CO_2 in kerogens using grand canonical Monte Carlo (GCMC) simulations.[26−30] Huang et al.[29] investigated the effect of moisture on the CO_2/CH_4 competitive adsorption in kerogen matrix and found that the increased moisture content leads to a decrease in adsorption capacity, and the CO_2/CH_4 adsorption selectivity first decreases and then increases. However, most of the work focused on the adsorption inside the kerogen matrix, in which the pores are isolated and not well connected, and the pore size is only a few angstroms. Recently, Wang et al.[31] studied the adsorption of CH_4/CO_2 mixtures in moist kerogen using a 2 nm wide slit-pore model and stated that the effect of moisture content on adsorption selectivity is not obvious for shale kerogen slit nanopores. A more realistic kerogen pore structure is used in their study, but the water molecules are placed inside the kerogen matrix rather than within the slit pores. The interaction between water and the adsorbate gas, which is mainly located in the slit pores, is weakened due to the separation. Therefore, the moisture effects on the adsorption of CH_4 and CO_2 are still not fully understood. In addition, the dependence of adsorption selectivity on pressure and pore size is extensively used in the previous research.[29−32] To some extent, it can imply the relative adsorption affinity of CH_4 and CO_2 to the adsorbent but fails to reflect the shale gas recovery process with CO_2 injection, namely, CO_2 huff-n-puff process, consisting of three stages: CO_2 injection, soaking, and production.[6] CO_2 is first injected into the production well (huff) and then the well is shut in and soaks for a period; finally comes the production (puff).[6]

In this work, we aim to reveal the effects of moisture on the competitive adsorption of CH_4/CO_2 binary mixtures in kerogen using GCMC simulations. Kerogen slit-pore models of different pore widths are constructed to represent the pore structure in shale.[33,34] First, we analyze the adsorption of pure methane in kerogen slit pores with and without the presence of moisture under a wide range of pressures from 10 to 60 MPa. Then, we discuss the moisture effects on the adsorption of CH_4/CO_2 binary mixtures in detail. Finally, we simulate the enhanced shale gas recovery by CO_2 huff-and-puff and compare the mechanisms of the pressure drawdown and CO_2 injection processes on shale gas recovery. The effects of moisture on the shale gas recovery and CO_2 sequestration are also revealed.

2. METHODS

2.1. Molecular Models. Kerogen can be classified into four types according to the depositional origin.[35,36] Type II kerogen, typically derived from marine sediments, is selected in this work for its abundance in shale deposits, as well as good potential for generating oil/gas.[37−39] The kerogen molecular unit (type II-C) used in the simulations was proposed by Ungerer et al.[40] on the basis of experimental data from the Duvernay shale formation.[41] Besides, type II-D kerogen has also been used to study the shale gas sorption behavior.[42]

Molecular dynamics (MD) simulations are conducted in the canonical ensemble (NVT) and isobaric−isothermal ensemble (NPT) using the large-scale atomic/molecular massively parallel simulator (LAMMPS) package[43] to generate kerogen matrixes and slit pores. The Dreiding force field[44] is employed to describe the kerogen properties. First, the initial structure of the kerogen macromolecule is relaxed individually. Then, 12 relaxed kerogen units are randomly placed in a simulation box of 100 × 100 × 100 Å^3. The final configuration of the kerogen matrix was created through a series of annealing procedures, as reported in Collell et al.[45] The density of the simulated kerogen matrix is 1.22 ± 0.02 g/cm^3, which is within the range of the experimental value of mature shales (1.18−1.35 g/cm^3).[46] The pore size distribution of the kerogen matrix is presented in Figure S1, calculated by the method of sphere insertion proposed by Bhattacharya and Gubbins.[47] Finally, we extend the simulation box in the Z-direction to create a kerogen slit nanopore, as shown in Figure 1. Note that we use the slit-shaped pore model as slit pores are very common in shale formations.[33,34] The pore width W is defined as the distance between the rightmost atom in the left slab and the leftmost atom in the right slab in the Z-direction. Two pore widths of 2 and 4 nm are constructed to investigate the pore size effects.

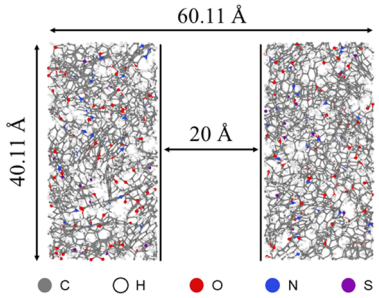

Figure 1. Atomistic model of kerogen slit nanopore. The pore width is 2 nm. Carbon atoms are depicted by gray balls, hydrogen by white, oxygen by red, nitrogen by blue, and sulfur by purple.

Methane molecules are simulated using TraPPE force field, and the united-atom model is applied.[48] The carbon dioxide molecule is treated as a rigid and linear structure with TraPPE-EH force field, where the C−O bond length and O−C−O bond angle are fixed as 1.16 Å and 180°, respectively.[49] The SPC/E model[50] is chosen for water with the O−H bond length of 1 Å and the H−O−H angle of 109.47°. Interaction between two atoms is calculated by the sum of Lennard-Jones (LJ) and electrostatic potential energy

$$u(r_{ij}) = 4\varepsilon_{ij}\left[\left(\frac{\sigma_{ij}}{r_{ij}}\right)^{12} - \left(\frac{\sigma_{ij}}{r_{ij}}\right)^{6}\right] + k_e\frac{q_i q_j}{r_{ij}} \quad (1)$$

DOI: 10.1021/acs.langmuir.9b00862
Langmuir 2019, 35, 8716−8725

where r_{ij} is the distance between atoms i and j; ε_{ij} and σ_{ij} represent the LJ potential well depth and the zero-potential distance, respectively; q is the charge of atoms; and $k_e = 8.988 \times 10^9$ N·m^2·C^{-2} is the electrostatic constant. The force field parameters are listed in Table 1.

Table 1. Force Field Parameters for Methane, Carbon Dioxide, and Water

atom	ε (K)	σ (Å)	q (e)
methane			
CH_4	148	3.73	0
carbon dioxide			
C	27	2.80	0.70
O	79	3.05	−0.35
water			
H	0	0	0.4238
O	78.18	3.166	−0.8476

Lorentz−Bertherlot mixing rules[51] are adopted to calculate interactions between unlike atoms. A cutoff distance of 14 Å is employed for short-range Lennard-Jones interactions, and analytical tail corrections are applied.[52] As our system has a finite length along the Z-direction, the conventional three-dimensional Ewald summation technique is not valid for the calculation of the long-range electrostatic interactions. Here, we use the same approach as for the three-dimensional Ewald summation, but an empty space is inserted between periodic replicas to avoid the artificial influence from the periodic images in the Z-direction.[52,53] Tests are carried out to ensure the length of the empty space is long enough that the artificial effects could be eliminated. The entire simulation box including the empty space is shown in Figure S2. During the simulations, the molecules are only allowed to move within the kerogen slit pore, but not into the vacuum.

2.2. Simulation Details. GCMC simulations are carried out in the grand canonical ensemble (μVT) to investigate the adsorption of CH_4 and CO_2 in kerogen slit pores. In the GCMC simulations, gases inside the kerogen slit pores are assumed to be in equilibrium with an external bulk reservoir under the same temperature and chemical potentials. The equilibration process is achieved by performing insertion, deletion, and translation moves for the gas molecules. For CO_2 and H_2O molecules, rotational moves are also applied. The chemical potentials are obtained by Widom's insertion method[54,55] using Monte Carlo simulations in the NVT ensemble, where the fluids are simulated in bulk phase without confinement. The calculated chemical potential values are verified by μVT simulations compared to those of NIST database[56] (Figure S3). The bulk densities of CO_2 and CH_4 mixtures at a given pressure and temperature are calculated from the Peng−Robinson equation of state (PR-EOS).[57,58] Bulk densities calculated by PR-EOS have been verified by comparing μVT simulations, as shown in Figure S4. MCCCS Towhee, a Monte Carlo molecular simulation code, is utilized in all of the GCMC simulations.[59]

During the GCMC simulations, the kerogen slit is kept rigid, but the water molecules are allowed to move. The number of water molecules is kept constant, based on the assumption that the water molecules remain in the pore during the shale gas recovery process. Besides, the water content is reported as the volumetric mass density of water, $\rho^{ave}_{H_2O}$, in the kerogen slit pore with the unit of g/cm^3. The pressure in the simulations denotes the pressure of the external bulk reservoir, which is in equilibrium with the confined system.

3. RESULTS AND DISCUSSION

In this section, we first investigate the adsorption of pure CH_4 and CH_4/CO_2 binary mixtures in kerogen slit pores, and the moisture effects are analyzed in detail. Then, we discuss the practical implications for the shale gas recovery and CO_2 sequestration during the CO_2 huff-and-puff process.

3.1. Adsorption of Pure CH_4 in Kerogen. *3.1.1. Dry Condition.* We present methane density distributions in various nanopores under dry conditions at 338.15 K in Figure 2. For all of the pressures, two strong methane adsorption layers are formed near the kerogen surfaces, and the methane density within the adsorption layer increases with pressure. Under higher pressures (over 10 MPa), the CH_4−CH_4 interaction becomes stronger and a weak second adsorption layer can be observed. In the middle of kerogen slit pores, the methane density is higher in the smaller pore (W = 2 nm) due to the strong fluid−surface interactions. As the pore width increases (W = 4 nm), the fluid−surface interaction becomes weaker. As a result, the methane density in the middle of the kerogen slit pore reaches bulk.

3.1.2. Moist Condition. To investigate the moisture effects on methane adsorption in kerogen, the methane adsorption under different moisture contents is simulated. The snapshots of CH_4 and H_2O molecules in the moist kerogen slit pores ($\rho^{ave}_{H_2O}$ 0.186 g/cm^3) under different pressures are shown in Figure 3. For all of the pressure conditions ranging from 10 to 60 MPa, water molecules form clusters in the middle of the kerogen slit pore, unlike in clay nanopores.[60] This is because the kerogen is hydrophobic, while the clay is hydrophilic. Similar phenomena were also reported on graphene and montmorillonite.[61]

The effects of water on the methane density distribution in 2 nm kerogen slit pores under different pressures are presented in Figure 4. In general, the CH_4 density in the middle of the kerogen slit pore decreases significantly as water molecules are predominantly distributed in the middle of the pore in the form of clusters. The methane density distribution in the

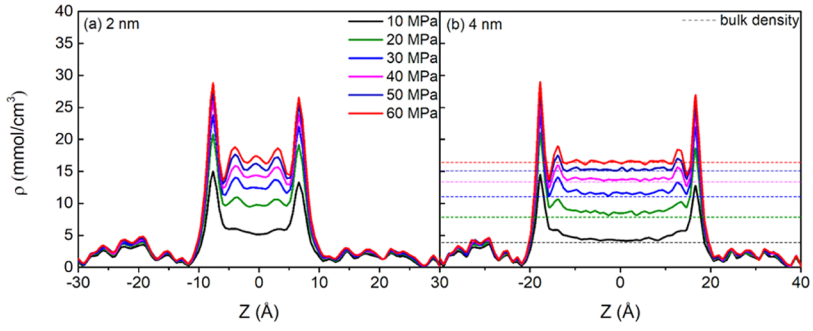

Figure 2. Methane density distributions in (a) 2 nm and (b) 4 nm kerogen slit pores under various bulk pressures and T = 338.15 K. Dashed lines represent the CH_4 bulk density obtained from the NIST Chemistry Webbook.[56]

DOI: 10.1021/acs.langmuir.9b00862
Langmuir 2019, 35, 8716−8725

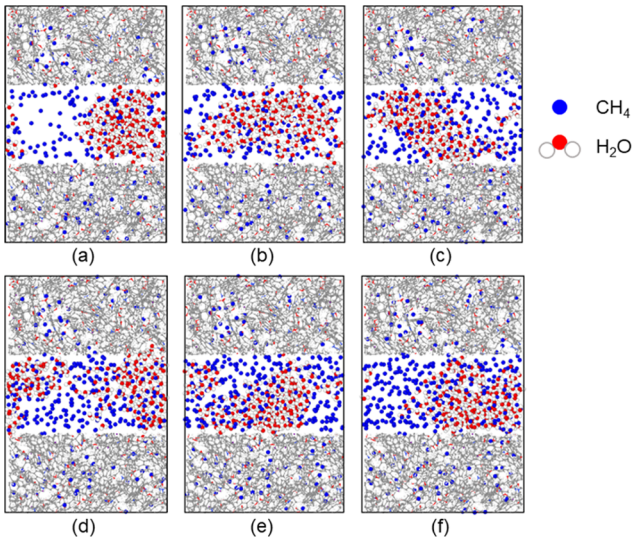

Figure 3. Snapshots of CH_4 and H_2O molecules in a 2 nm kerogen slit nanopore at 338.15 K under different pressures: (a) 10, (b) 20, (c) 30, (d) 40, (e) 50, and (f) 60 MPa with an average water density of 0.186 g/cm^3.

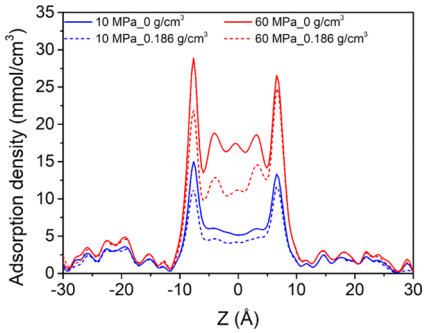

Figure 4. Methane density distributions in a 2 nm kerogen slit nanopore at different pressures: P = 10 MPa (blue) and 60 MPa (red), T = 338.15 K. The solid and dashed lines represent the CH_4 density distribution under dry condition (ρ^{ave}_{H2O} = 0 g/cm^3) and moist condition (ρ^{ave}_{H2O} = 0.186 g/cm^3), respectively.

presence of water is not symmetric because the water cluster is not located exactly at the center of the slit pore. For methane within the adsorption layer, the density also slightly decreases. From the water density distribution (as shown in Figure S5), some water molecules are distributed near the kerogen surface, occupying the adsorption sites on the surface and resulting in the decrease of methane in the adsorption layer.

The average density of methane stored in the kerogen slit pore can be given as

$$\rho_{ave} = \frac{\langle N \rangle}{V \cdot N_A} \quad (2)$$

where $\langle N \rangle$ is the ensemble averaged number of methane molecules in kerogen slit pores, V denotes the volume of the slit pore, and N_A is the Avogadro constant. We only consider the methane molecules in slit pores, excluding those inside the kerogen matrix. Figure 5 shows the total uptake of CH_4 at 338.15 K in kerogen slit pores of different pore widths with and without moisture. Statistical uncertainties on the sorption isotherms are examined, and the errors bars are less than the symbols. For both pore widths, the amount of adsorbed methane decreases monotonically with increasing water content. As shown in Figure 3, the water molecules are distributed in the middle of the slit pore in the form of clusters and occupy a fraction of the pore volume. Thus, they impede the pore filling of methane molecules in the middle of the pore. By comparing the CH_4 total uptakes in different pores (Figure 5), the reduction in the average density of methane is similar for 2 and 4 nm kerogen slit pores, when they have the same water volumetric density ($\rho^{ave}_{H_2O}$ 0.186 g/cm^3) rather than the same surface density. It demonstrates that the volumetric density of water may be more appropriate to define the water content in kerogen to quantify the effect of moisture on gas adsorption. CH_4 excess sorption isotherms in 2 and 4 nm dry kerogen slit pores are also calculated using effective pore volume from helium adsorption,[62] and the results are shown in Figure S6. It first reaches a maximum at around 15 MPa and then decreases with increasing pressure. Excess sorption in 2 nm kerogen slit pores is larger than that in 4 nm kerogen slit pores due to the stronger fluid−wall interaction.

3.2. Adsorption of CH_4/CO_2 Mixtures in Kerogen.

3.2.1. Dry Condition. The density distributions of CH_4 and CO_2 in the equimolar mixtures at 10 MPa and 338.15 K in kerogen slit pores of different pore widths are presented in Figure 6. The density distributions of both CO_2 and CH_4 have two peaks near the kerogen walls, but the density of CO_2 is much higher than that of CH_4, as CO_2 has a stronger affinity to kerogen than CH_4.[63] In the middle of 2 nm kerogen pores, both the densities of CO_2 and CH_4 are higher than the bulk density due to the strong fluid−surface interactions. When W = 4 nm, the fluid−surface interaction becomes weaker. Therefore, the densities in the middle of pores approach the

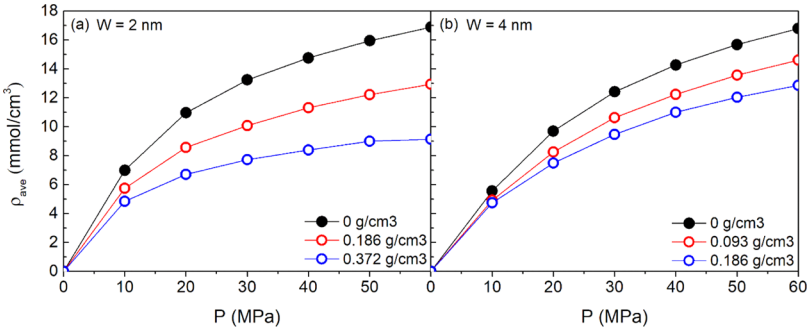

Figure 5. Average density of methane confined in kerogen slit pores with pore widths (a) 2 nm and (b) 4 nm at 338.15 K. The black, red, and blue lines represent the CH_4 adsorption at the dry condition and moist condition of different contents.

DOI: 10.1021/acs.langmuir.9b00862
Langmuir 2019, 35, 8716−8725

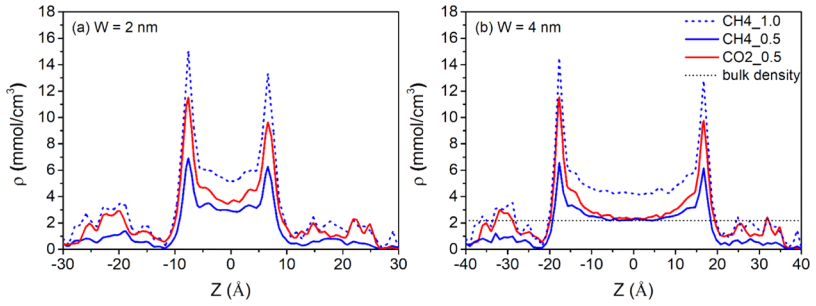

Figure 6. Density distributions of CH_4 and CO_2 molecules at 10 MPa and 338.15 K, respectively, in kerogen slit pores of widths (a) 2 nm and (b) 4 nm. The blue dashed lines represent the CH_4 density distribution in single-component adsorption and the solid lines represent the CH_4 and CO_2 density distributions in a binary mixture with a mole fraction of 0.5. The black dashed lines represent the bulk density of CH_4/CO_2.

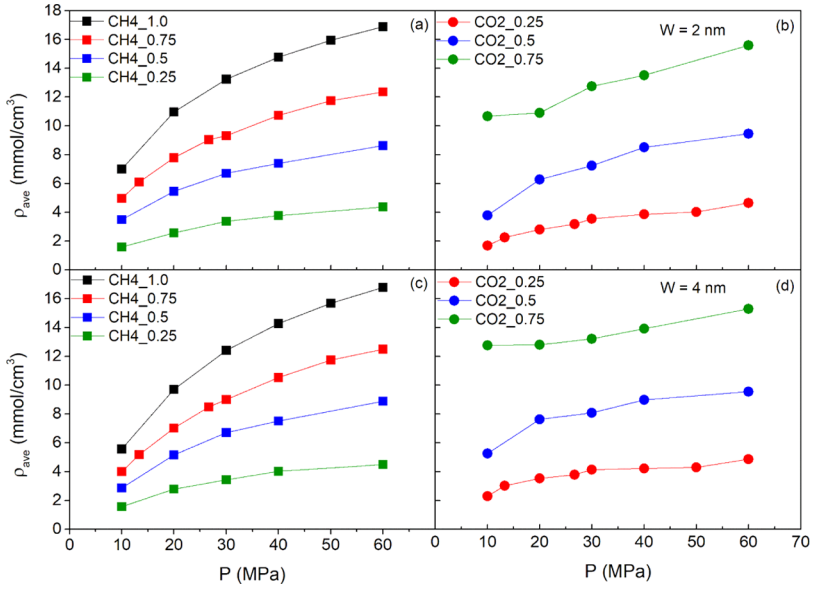

Figure 7. Average density of CH_4 (left) and CO_2 (right) in mixtures of different compositions confined in kerogen slit pores with pore widths of 2 nm (top) and 4 nm (bottom) under different pressures at 338.15 K.

bulk density. The density distributions of pure methane in kerogen slit pores under the same pressure are also shown in Figure 6 for comparison. With the competitive adsorption of CO_2, the density of methane decreases significantly, especially on the adsorption layer.

Figure 7 displays the total uptake of CH_4-CO_2 binary mixtures of different compositions in the dry kerogen slit pores of different pore widths at 338.15 K and over a wide range of pressures from 10 to 60 MPa. Similar trends can be observed for CH_4 in the kerogen slit pores of different pore widths that the average density increases quickly with pressure at the beginning and gradually reaches a plateau. The average density of CH_4 in kerogen slit pores increases as its mole fraction in the mixtures increases. For CO_2 molecules, sorption increases gradually with the increasing pressure. Similar to CH_4, as the mole fraction of CO_2 in the binary mixtures increases, an increase in the corresponding CO_2 adsorption can be observed. In the equimolar mixtures, the CO_2 average density in kerogen slit pores is much higher than that of CH_4.

3.2.2. Moist Condition. Sorption of CH_4/CO_2 binary mixtures in the moist kerogen slit pores is also investigated using GCMC simulations. As shown in Figure 8, water clusters are formed in the kerogen slit pores with the sorption of CH_4/CO_2 binary mixtures under pressures ranging from 10 to 60 MPa as pure CH_4 sorption with moisture. When there is only

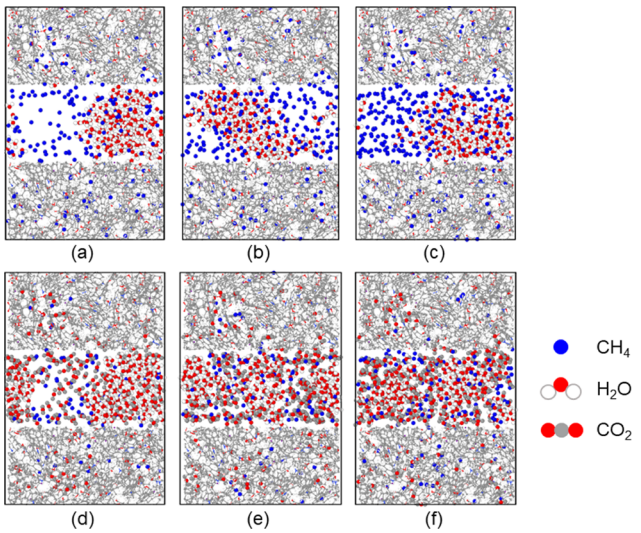

Figure 8. Snapshots of CH_4/H_2O mixtures (top) and $CH_4/CO_2/H_2O$ mixtures (bottom) in 2 nm kerogen slit nanopores at 338.15 K under different bulk pressures: 10, 30, and 60 MPa from left to right with an average water density of 0.186 g/cm^3. The mole fraction of CH_4 in the CH_4/CO_2 binary mixtures is 0.5.

DOI: 10.1021/acs.langmuir.9b00862
Langmuir 2019, 35, 8716−8725

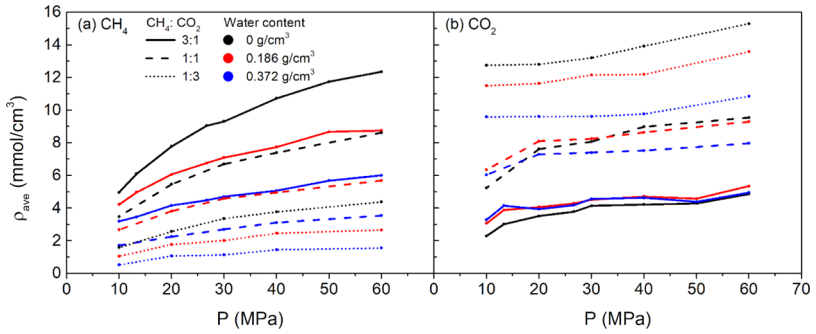

Figure 9. Total uptake of (a) CH_4 and (b) CO_2 molecules in mixtures of different compositions at 338.15 K in 2 nm kerogen slit nanopores with different moisture contents. The solid lines represent the mixtures with mole fractions of CH_4/CO_2 = 3:1, dashed lines CH_4/CO_2 = 1:1, and dotted lines CH_4/CO_2 = 1:3. The different colors represent different water contents: black for ρ^{ave}_{H2O} = 0 g/cm^3, red for ρ^{ave}_{H2O} = 0.186 g/cm^3, blue for ρ^{ave}_{H2O} = 0.372 g/cm^3.

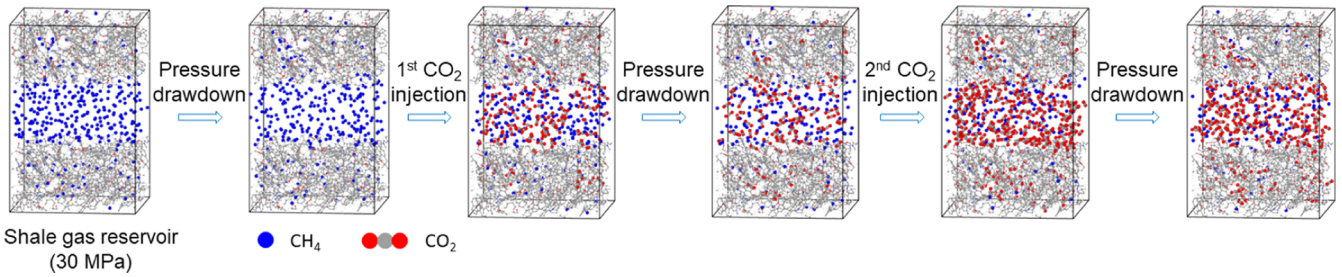

Figure 10. Schematic representation of the shale gas recovery process. More information about the recovery process is provided in the Supporting Information.

methane sorption in the moist kerogen slit pore, the pore surface is occupied by methane molecules. With the CO_2 cosorption, the adsorption sites on the kerogen surface are mainly covered by CO_2 molecules. Besides, the solubility of methane in water is much lower than that of CO_2.[64] As a result, CH_4 sorption in the moist condition is significantly reduced due to the cosorption of CO_2.

Effects of moisture contents on the total uptake of CH_4/CO_2 binary mixtures are illustrated in Figure 9. Similar to the trends in dry conditions, the average densities of both CH_4 and CO_2 in moist kerogen slit pores increase when their mole fraction increases. As the moisture content increases, the methane average density decreases significantly, independent of its mole fraction in the mixtures (Figure 9a). However, the effect of moisture content on CO_2 adsorption is associated with the mole fraction of CO_2 in the binary mixtures. For the case of low CO_2 bulk mole fraction in mixtures (y_{CO_2} = 0.25), a slight increase in CO_2 adsorption can be found in the moist condition, while the opposite is true at high CO_2 mole fraction (y_{CO_2} = 0.75). As stated in the previous section, the presence of moisture fills up the pore volume in kerogen slit pores, which results in the reduction in CH_4 sorption. With the CO_2 cosorption, the water−CH_4 binary interaction turns into the water−CH_4−CO_2 ternary interaction. Since the water−CO_2 interaction is much stronger than the water−CH_4 interaction, the decrease in accessible pore volumes for CH_4 can partially be occupied by the more favorable CO_2 sorption. Besides, within the region near the kerogen surface, CO_2 exhibits a higher affinity to kerogen compared to CH_4. Therefore, the CO_2 has a competitive advantage over CH_4 both in the middle of the kerogen slit pore and near the surface, which are shown in the snapshots (Figure 8) and density profiles (Figure S7). When the bulk mole fraction of CH_4 is relatively high, the decrease in methane sorption caused by the presence of water is pronounced. When the mole fraction of CO_2 is higher, both CO_2 and CH_4 need to compete with water for adsorption sites or space. The occupation of water in the kerogen slit pores limits the sorption of CO_2 and CH_4, thereby diminishing their sorption capacities. The sorption selectivity of CO_2 over CH_4 with different moisture contents is presented in Figure S8 to characterize the preferential adsorption. For the moisture contents considered in this work, the CO_2/CH_4 adsorption selectivity increases with increasing moisture content.

3.3. Implications for Shale Gas Recovery and CO_2 Storage. As outlined in the Introduction, this work aims to unravel the CH_4 recovery mechanisms under moist condition during the pressure drawdown process and CO_2 injection to investigate the recovery and sequestration efficiency. The simplified recovery process consists of two pressure drawdowns and two CO_2 injections, as illustrated in Figure 10. The initial pressure of the target shale gas reservoir is assumed to be 30 MPa, which is within the typical pressure range of realistic reservoir conditions. The CH_4 sorption amount in the kerogen slit pores is obtained by GCMC simulations. Then, the shale gas recovery is initiated by the primary pressure drawdown process, and the reservoir pressure is reduced to 20 MPa, while the amount of CH_4 residing in the kerogen slit pores is calculated via μVT simulation. Subsequently, CO_2 is injected into the shale gas reservoirs. During this process, we assume that the pore volume in the fractures (external bulk reservoir) remains the same; therefore, the CH_4 density in the bulk phase of CH_4/CO_2 mixtures is the same as that in pure CH_4. The resulting CH_4/CO_2 mixtures in the kerogen slit pores are determined by the chemical potentials of CH_4/CO_2 mixtures, which are obtained by NVT simulations. After the system has reached equilibrium, a pressure depletion process is applied

DOI: 10.1021/acs.langmuir.9b00862
Langmuir 2019, 35, 8716−8725

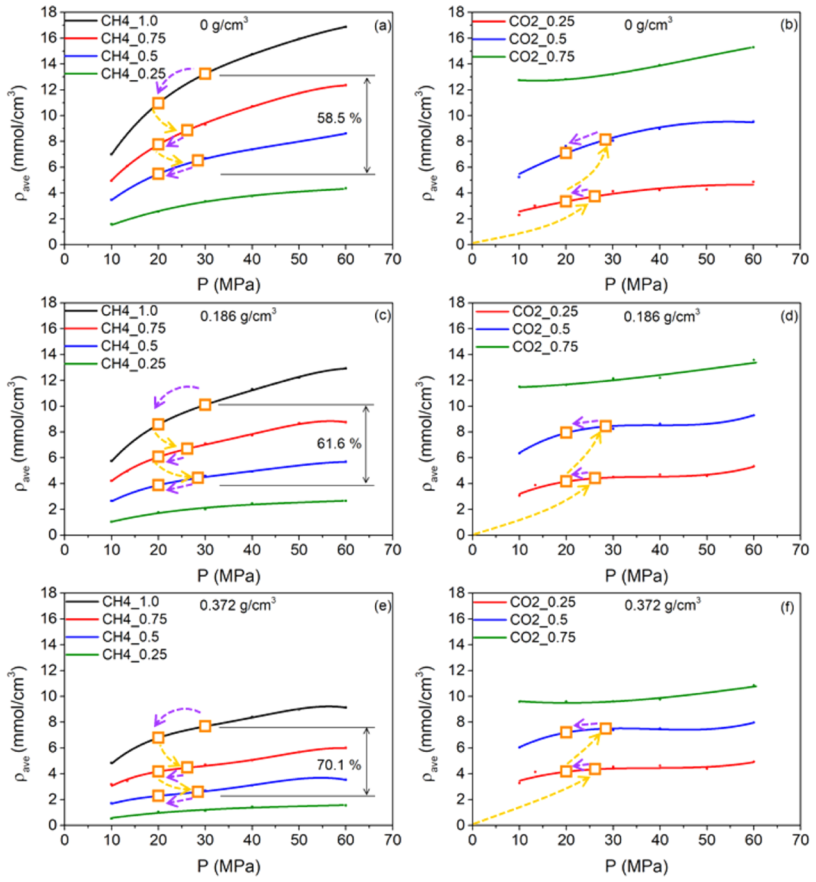

Figure 11. Composition of fluids in the 2 nm kerogen slit pores during the gas recovery process with different moisture contents: (a, b) 0 g/cm^3, (c, d) 0.186 g/cm^3, and (e, f) 0.372 g/cm^3. The arrows in the figure indicate the direction of the recovery process.

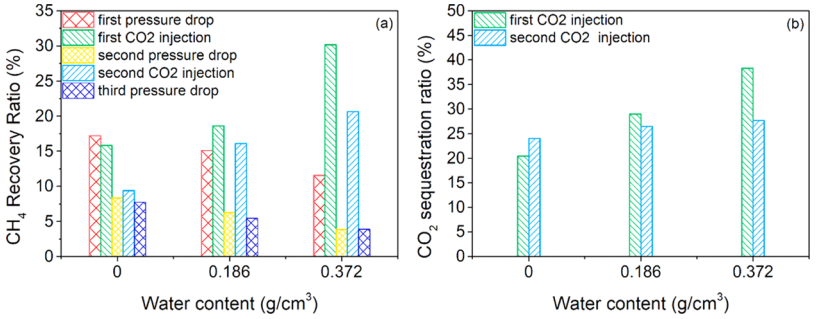

Figure 12. CH_4 recovery ratio (a) and CO_2 sequestration ratio (b) with respect to water content during the shale gas recovery process in 2 nm kerogen slit pores at 338.15 K.

again, while the bulk CH_4/CO_2 composition stays the same. The dynamics and transport processes are not considered.[65] This process achieves one cycle of CO_2 huff-n-puff in enhanced gas recovery.[6,66] Consequently, a second CO_2 huff-n-puff process is operated.

Evolution in the composition of fluids in the kerogen slit pores during the shale gas recovery process is shown in Figure 11. During the pressure drawdown, the average CH_4 density in the kerogen slit pores decreases continuously, and with the injection of CO_2, the CH_4 molecules are further released. The CO_2 molecules are sequestrated in the kerogen slit pores after injection. The effects of moisture content are also shown in Figure 11; as the moisture content increases, the average density of methane at the initial stage is reduced from 13.2 mmol/cm^3 in the dry condition to 7.68 mmol/cm^3 with an average water density of 0.372 g/cm^3, but the recovery ratio of CH_4 after the whole recovery process is increased from 58.5 to 70.1%.

To compare the efficiency of the shale gas recovery and CO_2 sequestration during every intermediate process and quantify the effects of moisture contents, we introduce two parameters: CH_4 recovery ratio and CO_2 sequestration ratio, taking the initial pressure (30 MPa) of the reservoir as the reference. The CH_4 recovery ratio is defined as the number of CH_4 molecules released during a single process relative to the initial amount in the kerogen slit pore under 30 MPa with/without moist. The CO_2 sequestration ratio is defined as the number of CO_2 molecules sequestrated during the CO_2 injection process relative to its adsorption amount in the kerogen slit pore under 30 MPa, namely, the maximum amount of CO_2 sequestration

DOI: 10.1021/acs.langmuir.9b00862
Langmuir 2019, 35, 8716−8725

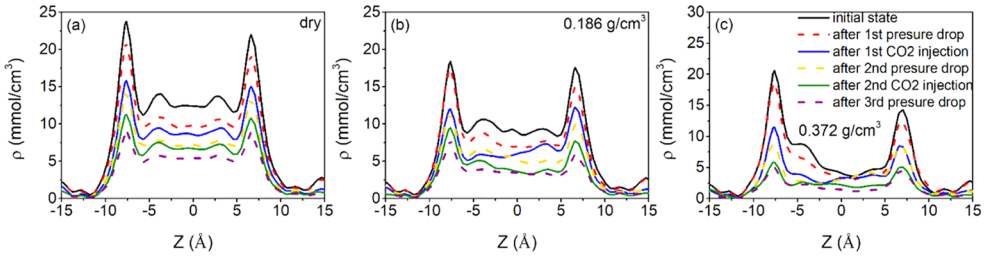

Figure 13. Evolution of the CH_4 density distributions inside the 2 nm kerogen slit pores during the gas recovery process with varying moisture contents: (a) 0 g/cm^3, dry condition (b) 0.186 g/cm^3, and (c) 0.372 g/cm^3. The CO_2 density distribution during the CO_2 injection process is presented in Figure S10.

in a 30 MPa reservoir with/without moist. The CO_2 sequestration ratio can serve as a parameter for indicating the extent of CO_2 sequestration. The two parameters are plotted as a percentage in Figure 12 under different moisture contents. As can be seen from Figure 12a, as the moisture content increases, the CH_4 recovery ratio of the pressure drawdown processes decreases, while that of CO_2 injection processes increases, which means in the moist conditions, the performance of the CO_2 injection method can be even better, while the efficiency of the pressure drop method is lowered. In the dry conditions (0 g/cm^3), the first pressure drawdown process accounts for the largest proportion of the total amount of shale gas recovered, while in the moist conditions, the CH_4 recovery ratio of the first CO_2 injection process is the largest over the whole recovery process. To clarify the role of CO_2 injection in the recovery process, we calculate the recovery ratio of the process with the pressure drawdown only from 30 to 20 MPa. The recovery ratios between the two processes are compared (Figure S9). With the combination of CO_2 injection, recovery ratios are enhanced by 2.4, 3.1, and 5.1 times for water densities of 0, 0.186, and 0.372 g/cm^3, respectively. For the CO_2 sequestration during the CO_2 injection process (Figure 12b), the CO_2 sequestration ratio rises with increasing moisture content, especially in the first stage. A considerable CO_2 sequestration ratio of 63.4% in total can be achieved in the moist kerogen slit pores at an average water density of 0.372 g/cm^3.

To explain the different effects of moisture contents on the pressure drop method and CO_2 injection method, we further investigate the CH_4 recovery mechanisms of the two methods. The evolution of the CH_4 density distributions during the gas recovery process with different moisture contents is plotted in Figure 13. After the pressure drawdown, the CH_4 density in the middle of the kerogen slit pore is reduced, while after the CO_2 injection, the decrease in CH_4 density mainly occurs in the adsorption layer near the kerogen surface, indicating different mechanisms in shale gas recovery. In other words, the pressure drawdown releases the free gas in the middle of pores, while the CO_2 injection recovers CH_4 from the adsorption layers. In the presence of water in kerogen slit pores (Figure 13b,c), since the water molecules accumulate as clusters in the middle of kerogen slit pores, the moisture content negatively affects the performance of the pressure drawdown. Meanwhile, the adverse effect of moisture on the CO_2 injection method is negligible, as the water−CO_2 interaction is much stronger than the water−CH_4 interaction. Hence, the presence of water could further improve the efficiency of the CO_2 injection method. Generally, in the moist conditions, the CO_2 injection behaves better, while the efficiency of the pressure drawdown is lower.

4. CONCLUSIONS

In this work, the effects of moisture on the adsorption of pure CH_4 and CH_4/CO_2 binary mixtures in kerogen slit pores are investigated using GCMC simulations. The shale gas recovery mechanisms of the pressure drawdown and CO_2 injection are studied, and the moisture effects on the shale gas recovery and CO_2 sequestration efficiency are further explored.

Our simulation results show that for the sorption of pure CH_4 in the moist conditions, water clusters are formed in the middle of a kerogen slit pore and the clusters occupy the volume in the slit pore, thereby impeding the pore filling of CH_4. Regarding the sorption of CH_4/CO_2 binary mixture, the CH_4 sorption capacity in the mixture decreases with increasing moisture content, while the effect of moisture on CO_2 adsorption capacity depends on the mole fraction of CO_2 in the mixture due to the ternary interactions among CH_4, CO_2, and H_2O. During the shale gas recovery process, the pressure drawdown and CO_2 injection present different mechanisms. The pressure drawdown releases CH_4 molecules in the middle of kerogen slit pores, while CO_2 injection can release CH_4 molecules in the adsorption layer. As the water content increases, the recovery ratio of the pressure drawdown declines, while that of CO_2 injection increases, especially in the first stage of CO_2 injection. Finally, the CO_2 sequestration efficiency is higher under moist conditions.

This work provides important insights into the effects of moisture content on gas adsorption in kerogen. As the subsurface water in the shale formations is saline, further work is planned to examine the effects of saline water on the recovery process. Besides, the recovery process introduced in this work can be extended to the optimization of the shale gas recovery process. For example, adjusting the CO_2 injection pressure and depletion pressure may lead to optimal shale gas recovery efficiency or CO_2 sequestration efficiency. The recovery process can also be applied to other displacement processes in confined systems.

■ ASSOCIATED CONTENT

Supporting Information

The Supporting Information is available free of charge on the ACS Publications website at DOI: 10.1021/acs.langmuir.9b00862.

Chemical potentials of pure methane and mixtures (Table S1); additional details of bulk fluids (Table S2); pore size distribution of the kerogen matrix (Figure S1); entire simulation box (Figure S2); densities of bulk CH_4 (Figure S3); validation of the PR-EOS (Figure S4); water density distributions (Figure S5); CH_4 excess adsorption isotherms (Figure S6); density distributions

DOI: 10.1021/acs.langmuir.9b00862
Langmuir 2019, 35, 8716−8725

(Figure S7); CO_2/CH_4 adsorption selectivity (Figure S8); total shale gas recovery ratio (Figure S9); and CO_2 density distributions (Figure S10)

AUTHOR INFORMATION

Corresponding Authors

*E-mail: zhehui2@ualberta.ca. Fax: +1 780-492-6633.
*E-mail: K.Luo@ucl.ac.uk. Fax +44 (0)20 7388 0180.

ORCID

Zhehui Jin: 0000-0001-8305-5637
Kai H. Luo: 0000-0003-4023-7259

Notes

The authors declare no competing financial interest.

ACKNOWLEDGMENTS

Support from the MOST National Key Research and Development Programme (Project No. 2016YFB0600805) and the Center for Combustion Energy at Tsinghua University is gratefully acknowledged. The simulations were partly performed on the High-Performance Parallel Computer supported by the Tsinghua HPC Platform. Additional support from the UK Engineering and Physical Sciences Research Council under the project UK Consortium on Mesoscale Engineering Sciences (UKCOMES) (Grant No. EP/R029598/1) is gratefully acknowledged. Z.J. acknowledges a Discovery Grant from the Natural Sciences and Engineering Research Council of Canada (NSERC RGPIN-2017-05080).

REFERENCES

(1) Vidic, R. D.; Brantley, S. L.; Vandenbossche, J. M.; Yoxtheimer, D.; Abad, J. D. Impact of Shale Gas Development on Regional Water Quality. *Science* **2013**, *340*, No. 1235009.

(2) Melikoglu, M. Shale Gas: Analysis of Its Role in the Global Energy Market. *Renewable Sustainable Energy Rev.* **2014**, *37*, 460−468.

(3) Arogundade, O.; Sohrabi, M. A Review of Recent Developments and Challenges in Shale Gas Recovery, *SPE Saudi Arabia Section Technical Symposium and Exhibition*, 8−11 April 2012, Al-Khobar, Saudi Arabia, 2012.

(4) Middleton, R.; Viswanathan, H.; Currier, R.; Gupta, R. CO_2 as a Fracturing Fluid: Potential for Commercial-Scale Shale Gas Production and CO2 Sequestration. *Energy Procedia* **2014**, *63*, 7780−7784.

(5) Yang, R.; Goktekin, E.; Gleason, K. K. Zwitterionic Antifouling Coatings for the Purification of High-Salinity Shale Gas Produced Water. *Langmuir* **2015**, *31*, 11895−11903.

(6) Yu, W.; Lashgari, H.; Sepehrnoori, K. Simulation Study of CO2 Huff-n-Puff Process in Bakken Tight Oil Reservoirs, *SPE Western North American and Rocky Mountain Joint Meeting*, Society of Petroleum Engineers, 17−18 April, Denver, Colorado, 2014.

(7) Loring, J. S.; Ilton, E. S.; Thompson, C. J.; Martin, P. F.; Rosso, K. M.; Felmy, A. R.; Schaef, H. T.; et al. In Situ Study of CO2 and H2O Partitioning between Na−Montmorillonite and Variably Wet Supercritical Carbon Dioxide. *Langmuir* **2014**, *30*, 6120−6128.

(8) Wang, X. H.; Sun, Y. F.; Wang, Y. F.; Li, N.; Sun, C. Y.; Chen, G. J.; Liu, B.; Yang, L. Y. Gas Production from Hydrates by CH4-CO2/H2 Replacement. *Appl. Energy* **2017**, *188*, 305−314.

(9) Vandenbroucke, M.; Largeau, C. Kerogen Origin, Evolution and Structure. *Org. Geochem.* **2007**, *38*, 719−833.

(10) Ortiz Cancino, O. P.; Peredo Mancilla, D.; Pozo, M.; Pérez, E.; Bessieres, D. Effect of Organic Matter and Thermal Maturity on Methane Adsorption Capacity on Shales from the Middle Magdalena Valley Basin in Colombia. *Energy Fuels* **2017**, *31*, 11698−11709.

(11) Parfenova, T. M.; Kontorovich, A. E.; Borisova, L. S.; Melenevskii, V. N. Kerogen from the Cambrian Deposits of the Kuonamka Formation (Northeastern Siberian Platform). *Russ. Geol. Geophys.* **2010**, *51*, 277−285.

(12) Chalmers, G. R.; Bustin, M. R. The Effects and Distribution of Moisture in Gas Shale Reservoirs Systems, *AAPG Annual Convention and Exhibition*, New Orleans, Louisiana, April 11−14, 2010.

(13) Ruppert, L. F.; Sakurovs, R.; Blach, T. P.; He, L.; Melnichenko, Y. B.; Mildner, D. F. R.; Alcantar-Lopez, L. A USANS/SANS Study of the Accessibility of Pores in the Barnett Shale to Methane and Water. *Energy Fuels* **2013**, *27*, 772−779.

(14) Ross, D. J. K.; Bustin, R. M. The Importance of Shale Composition and Pore Structure upon Gas Storage Potential of Shale Gas Reservoirs. *Mar. Pet. Geol.* **2009**, *26*, 916−927.

(15) Zhang, T.; Ellis, G. S.; Ruppel, S. C.; Milliken, K.; Yang, R. Effect of Organic-Matter Type and Thermal Maturity on Methane Adsorption in Shale-Gas Systems. *Org. Geochem.* **2012**, *47*, 120−131.

(16) Li, X.; Krooss, B. M. Influence of Grain Size and Moisture Content on the High-Pressure Methane Sorption Capacity of Kimmeridge Clay. *Energy Fuels* **2017**, *31*, 11548−11557.

(17) Gasparik, M.; Bertier, P.; Gensterblum, Y.; Ghanizadeh, A.; Krooss, B. M.; Littke, R. Geological Controls on the Methane Storage Capacity in Organic-Rich Shales. *Int. J. Coal Geol.* **2014**, *123*, 34−51.

(18) Gensterblum, Y.; Busch, A.; Krooss, B. M. Molecular Concept and Experimental Evidence of Competitive Adsorption of H2O, CO2 and CH4 on Organic Material. *Fuel* **2014**, *115*, 581−588.

(19) Razavi, S.; Koplik, J.; Kretzschmar, I. Molecular Dynamics Simulations: Insight into Molecular Phenomena at Interfaces. *Langmuir* **2014**, *30*, 11272−11283.

(20) Rezlerová, E.; Zukal, A.; Cejka, J.; Siperstein, F. R.; Brennan, J. K.; Lisal, M. Adsorption and Diffusion of C1 to C4 Alkanes in Dual-Porosity Zeolites by Molecular Simulations. *Langmuir* **2017**, *33*, 11126−11137.

(21) Billemont, P.; Coasne, B.; Weireld, G. De Adsorption of Carbon Dioxide, Methane, and Their Mixtures in Porous Carbons: Effect of Surface Chemistry, Water Content, and Pore Disorder. *Langmuir* **2013**, *29*, 3328−3338.

(22) Brochard, L.; Vandamme, M.; Pellenq, R. J.; Fen-chong, T. Adsorption-Induced Deformation of Microporous Materials: Coal Swelling Induced by CO2−CH4 Competitive Adsorption. *Langmuir* **2012**, *28*, 2659−2670.

(23) Savoy, E. S.; Escobedo, F. A. Molecular Simulations of Wetting of a Rough Surface by an Oily Fluid: Effect of Topology, Chemistry, and Droplet Size on Wetting Transition Rates. *Langmuir* **2012**, *28*, 3412−3419.

(24) Wei, N.; Lv, C.; Xu, Z. Wetting of Graphene Oxide: A Molecular Dynamics Study. *Langmuir* **2014**, *30*, 3572−3578.

(25) Storm, S.; Jakobtorweihen, S.; Smirnova, I.; Panagiotopoulos, A. Z. Molecular Dynamics Simulation of SDS and CTAB Micellization and Prediction of Partition Equilibria with COSMOmic. *Langmuir* **2013**, *29*, 11582−11592.

(26) Sui, H.; Yao, J. Effect of Surface Chemistry for CH4/CO2 Adsorption in Kerogen: A Molecular Simulation Study. *J. Nat. Gas Sci. Eng.* **2016**, *31*, 738−746.

(27) Wang, T.; Tian, S.; Li, G.; Sheng, M. Selective Adsorption of Supercritical Carbon Dioxide and Methane Binary Mixture in Shale Kerogen Nanopores. *J. Nat. Gas Sci. Eng.* **2018**, *50*, 181−188.

(28) Song, R.; Cui, M. Molecular Simulation on Competitive Adsorption Mechanism of CH4/CO2 on Shale Kerogen. *Arab. J. Geosci.* **2018**, *11*, No. 403.

(29) Huang, L.; Ning, Z.; Wang, Q.; Zhang, W.; Cheng, Z.; Wu, X.; Qin, H. Effect of Organic Type and Moisture on CO2/CH4 Competitive Adsorption in Kerogen with Implications for CO2 Sequestration and Enhanced CH4 Recovery. *Appl. Energy* **2018**, *210*, 28−43.

(30) Huang, L.; Ning, Z.; Wang, Q.; Qi, R.; Zeng, Y.; Qin, H.; Ye, H.; Zhang, W. Molecular Simulation of Adsorption Behaviors of Methane, Carbon Dioxide and Their Mixtures on Kerogen: Effect of Kerogen Maturity and Moisture Content. *Fuel* **2018**, *211*, 159−172.

(31) Wang, T.; Tian, S.; Li, G.; Sheng, M.; Ren, W.; Liu, Q.; Zhang, S. Molecular Simulation of CO2/CH4 Competitive Adsorption on

DOI: 10.1021/acs.langmuir.9b00862
Langmuir 2019, 35, 8716−8725

Shale Kerogen for CO2 Sequestration and Enhanced Gas Recovery. *J. Phys. Chem. C* **2018**, *122*, 17009−17018.
(32) Sun, H.; Zhao, H.; Qi, N.; Li, Y. Molecular Insights into the Enhanced Shale Gas Recovery by Carbon Dioxide in Kerogen Slit Nanopores. *J. Phys. Chem. C* **2017**, *121*, 10233−10241.
(33) Chalmers, G. R.; Bustin, R. M.; Power, I. M. Characterization of Gas Shale Pore Systems by Porosimetry, Pycnometry, Surface Area, and Field Emission Scanning Electron Microscopy/Transmission Electron Microscopy Image Analyses: Examples from the Barnett, Woodford, Haynesville, Marcellus, and Doig Uni. *AAPG Bull.* **2012**, *96*, 1099−1119.
(34) Curtis, M. E.; Cardott, B. J.; Sondergeld, C. H.; Rai, C. S. International Journal of Coal Geology Development of Organic Porosity in the Woodford Shale with Increasing Thermal Maturity. *Int. J. Coal Geol.* **2012**, *103*, 26−31.
(35) McCarthy, K.; Rojas, K.; Niemann, M.; Palmowski, D.; Peters, K.; Stankiewicz, A. Basic Petroleum Geochemistry for Source Rock Evaluation. *Oilfield Rev.* **2011**, *23*, 32−43.
(36) Bousige, C.; Ghimbeu, C. M.; Vix-Guterl, C.; Pomerantz, A. E.; Suleimenova, A.; Vaughan, G.; Garbarino, G.; Feygenson, M.; Wildgruber, C.; Ulm, F. J.; et al. Realistic Molecular Model of Kerogen's Nanostructure. *Nat. Mater.* **2016**, *15*, 576−582.
(37) Tissot, B. P.; Welte, D. H. Petroleum Formation and Occurrence. *Trans., Am. Geophys. Union* **1985**, *66*, 643.
(38) Vandenbroucke, M. Kerogen: From Types to Models of Chemical Structure. *Oil Gas Sci. Technol.* **2003**, *58*, 243−269.
(39) Jarvie, D. M.; Hill, R. J.; Ruble, T. E.; Pollastro, R. M. Unconventional Shale-Gas Systems: The Mississippian Barnett Shale of North-Central Texas as One Model for Thermogenic Shale-Gas Assessment. *AAPG Bull.* **2007**, *91*, 475−499.
(40) Ungerer, P.; Collell, J.; Yiannourakou, M. Molecular Modeling of the Volumetric and Thermodynamic Properties of Kerogen: Influence of Organic Type and Maturity. *Energy Fuels* **2015**, *29*, 91−105.
(41) Kelemen, S. R.; Afeworki, M.; Gorbaty, M. L.; Sansone, M.; Kwiatek, P. J.; Walters, C. C.; Freund, H.; Siskin, M.; et al. Direct Characterization of Kerogen by X-Ray and Solid-State 13C Nuclear Magnetic Resonance Methods. *Energy Fuels* **2007**, *21*, 1548−1561.
(42) Michalec, L.; Lísal, M. Molecular Simulation of Shale Gas Adsorption onto Overmature Type II Model Kerogen with Control Microporosity. *Mol. Phys.* **2017**, *115*, 1086−1103.
(43) Plimpton, S. Fast Parallel Algorithms for Short-Range Molecular-Dynamics. *J. Comput. Phys.* **1995**, *117*, 1−19.
(44) Mayo, S. L.; Olafson, B. D.; Goddard, W. A. DREIDING: A Generic Force Field for Molecular Simulations. *J. Phys. Chem.* **1990**, *94*, 8897−8909.
(45) Collell, J.; Ungerer, P.; Galliero, G.; Yiannourakou, M.; Montel, F.; Pujol, M. Molecular Simulation of Bulk Organic Matter in Type II Shales in the Middle of the Oil Formation Window. *Energy Fuels* **2014**, *28*, 7457−7466.
(46) Okiongbo, K. S.; Aplin, A. C.; Larter, S. R. Changes in Type II Kerogen Density as a Function of Maturity: Evidence from the Kimmeridge Clay Formation. *Energy Fuels* **2005**, *19*, 2495−2499.
(47) Bhattacharya, S.; Gubbins, K. E. Fast Method for Computing Pore Size Distributions of Model Materials. *Langmuir* **2006**, *22*, 7726−7731.
(48) Martin, M. G.; Siepmann, J. I. Transferable Potentials for Phase Equilibria. 1. United-Atom Description of n-Alkanes. *J. Phys. Chem. B* **1998**, *102*, 2569−2577.
(49) Potoff, J. J.; Siepmann, J. I. Vapor-Liquid Equilibria of Mixtures Containing Alkanes, Carbon Dioxide, and Nitrogen. *AIChE J.* **2001**, *47*, 1676−1682.
(50) Grigera, J.; Berendsen, H. J. C.; Straatsma, T. P. The Missing Term in Effective Pair Potentials. *J. Phys. Chem.* **1987**, *91*, 6269−6271.
(51) Lorentz, H. A. Ueber Die Anwendung Des Satzes Vom Virial in Der Kinetischen Theorie Der Gase. *Ann. Phys.* **1881**, *248*, 127−136.
(52) Frenkel, D.; Smit, B. *Understanding Molecular Simulation: From Algorithms to Applications*; Elsevier, 2001; Vol. *1*.
(53) Shelley, J. C. Boundary Condition Effects in Simulations of Water Confined between Planar Walls. *Mol. Phys.* **1996**, *88*, 385−398.
(54) Widom, B. Potential-Distribution Theory and the Statistical Mechanics of Flulds. *J. Phys. Chem.* **1982**, *86*, 869−872.
(55) Widom, B. Some Topics in the Theory of Fluids. *J. Chem. Phys.* **1963**, *39*, 2808.
(56) Lemmon, E.; McLinden, M.; Huber, M.*NIST Reference Fluid Thermodynamic and Transport Properties—REFPROP*, v7. NIST standard reference database.
(57) Peng, D.; Robinson, D. B. A New Two-Constant Equation of State. *Ind. Eng. Chem. Fundam.* **1976**, *15*, 59−64.
(58) Kunz, O.; Klimeck, R.; Wagner, W.; Jaeschke, M. The GERG-2004 Wide-Range Equation of State for Natural Gases and Other Mixtures *GERG Tech. Monogr.* 2007.
(59) Martin, M. G. MCCCS Towhee: A Tool for Monte Carlo Molecular Simulation. *Molecular Simulation*; Taylor & Francis, 2013; pp 1212−1222.
(60) Jin, Z.; Firoozabadi, A. Effect of Water on Methane and Carbon Dioxide Sorption in Clay Minerals by Monte Carlo Simulations. *Fluid Phase Equilib.* **2014**, *382*, 10−20.
(61) Wang, S.; Feng, Q.; Zha, M.; Javadpour, F.; Hu, Q. Supercritical Methane Diffusion in Shale Nanopores: Effects of Pressure, Mineral Types, and Moisture Content. *Energy Fuels* **2018**, *32*, 169−180.
(62) Tian, Y.; Yan, C.; Jin, Z. Characterization of Methane Excess and Absolute Adsorption in Various Clay Nanopores from Molecular Simulation. *Sci. Rep.* **2017**, *7*, No. 12040.
(63) Kang, S. M.; Fathi, E.; Ambrose, R. J.; Akkutlu, I. Y.; Sigal, R. F. Carbon Dioxide Storage Capacity of Organic-Rich Shales. *SPE J.* **2011**, *16*, 842.
(64) Yamamoto, S.; Alcauskas, J. B.; Crozier, T. E. Solubility of Methane in Distilled Water and Seawater. *J. Chem. Eng. Data* **1976**, *21*, 78−80.
(65) Bui, K.; Akkutlu, I. Y. Hydrocarbons Recovery From Model-Kerogen Nanopores. *SPE J.* **2017**, *22*, 0854−0862.
(66) Meng, X.; Meng, Z.; Ma, J.; Wang, T. Performance Evaluation of CO2 Huff-n-Puff Gas Injection in Shale Gas Condensate Reservoirs. *Energies* **2019**, *12*, 1−18.

DOI: 10.1021/acs.langmuir.9b00862
Langmuir 2019, 35, 8716−8725